Article:
Bhattacharya, P., Kelleher, J.E. and Siegmund, T. (2015) Role of gradients in vocal fold elastic modulus on phonation. Journal of Biomechanics, 48 (12). pp. 3356-3363. ISSN: 0021-9290

https://doi.org/10.1016/j.jbiomech.2015.06.015

Role of gradients in vocal fold elastic modulus on phonation

Pinaki Bhattacharya, Jordan E. Kelleher, Thomas Siegmund*

School of Mechanical Engineering, Purdue University, West Lafayette, IN 47907 USA

Abstract

New studies show that the elastic properties of the vocal folds (VFs) vary locally. In particular strong gradients exist in the distribution of elastic modulus along the length of the VF ligament, which is an important load-bearing constituent of the VF tissue. There is further evidence that changes in VF health are associated with alterations in modulus gradients. The role of VF modulus gradation on VF vibration and phonation remains unexplored. In this study the magnitude of the gradient in VF elastic modulus is varied, and sophisticated computational simulations are performed of the self-oscillation of three-dimensional VFs with realistic modeling of airflow physical properties. Results highlight that phonation frequency, characteristic modes of deformation and phase differences, glottal airflow rate, spectral-width of vocal output, and glottal jet dynamics are dependent on the magnitude of VF elastic modulus gradation. The results advance the understanding of how VF functional gradation can lead to perceptible changes in speech quality.

Keywords: phonation, vocal fold biomechanics, functional property gradation, speech quality

1. Introduction

There is evidence that the vocal fold (VF) state of health influences the spatial distribution of VF elastic properties. Kelleher et al. (2012) show that gradients in elastic modulus are smaller in cover and ligament specimens excised from subjects associated with tobacco use than specimens excised from non-smokers. Kelleher et al. (2010) show that in vacuo eigenmodes of VF tissue are dependent on gradients in elastic modulus. Zhang et al. (2007) show in vacuo eigenmodes playing an important role in the onset of flow-structure interaction (FSI). These findings lead to the hypothesis that functional gradients in VF tissue modulus influence VF dynamics during self-sustained FSI. Answering this hypothesis would contribute to understanding why several studies report perceptible differences between speech quality of smokers and non-smokers.

A very limited number of studies conduct the simulation of VF self-oscillation under conditions of three-dimensional (3D) geometry and physically reasonable air flow and VF tissue properties. These conditions

*Corresponding author

Email address: siegmund@purdue.edu (Thomas Siegmund)

impose significant computational modeling challenges. Bhattacharya and Siegmund (2014b) demonstrate the use of commercially available dedicated solvers for flow and structural domains to solve problems of VF FSI including vibration and contact, VF dehydration (Bhattacharya and Siegmund, 2014a) and surface adhesion (Bhattacharya and Siegmund, 2015). Bhattacharya and Siegmund (2014c) validated this framework against experiments on physical replicas.

This study aims to obtain insights into the role of gradients in VF elastic modulus on VF dynamics during phonation. FSI simulations are conducted using a partitioned approach, whereby segregated solvers for the governing equations of the solid and fluid domains exchange information after every time increment. The investigation is limited to a linear elastic isotropic description of VF tissue properties situated within a 3D model of the glottal tract. The influence of gradation is quantified by analysing VF surface dynamics during phonation.

2. Method

2.1. Computational model

The VF model comprises separate continuum region definitions for the glottal airflow and the pair of VFs. The FSI model describes the interaction between each VF and the airflow (Bhattacharya and Siegmund, 2014b).

The M5 description (Scherer et al., 2001) defines the geometry of the airflow domain (figure 1a) with a rectangular x_{is}-x_{ml}-x_{ap} coordinate system aligned with inferior–superior (*is*), medial–lateral (*ml*) and anterior–posterior (*ap*) directions. The sub- and supra-glottal tracts have uniform rectangular cross-sectional dimensions (*ml*: $W = 17.4$ mm, *ap*: $L = 20.0$ mm) but unequal *is* dimensions ($T_{\mathrm{entry}} = 10.0$ mm and $T_{\mathrm{exit}} = 20.0$ mm respectively). The *is* dimension of the glottal region is $T = 10.7$ mm. The fluid medium has properties of air (constant density $\rho_f = 1.23$ kg/m^3, dynamic viscosity $\mu = 1.79 \cdot 10^{-5}$ kg/m·s) modeled as a Newtonian fluid with fluid stress $\boldsymbol{\tau}_f$ and fluid velocity $\vec{v}$ related by

$$\boldsymbol{\tau}_f = \mu \left[\nabla \vec{v} + (\nabla \vec{v})' \right]. \tag{1}$$

The continuity and momentum conservation equations are

$$0 = \oint_{\partial(V^f)} (\vec{v} - \vec{v}_g) \cdot \mathrm{d}\vec{S} \tag{2}$$

$$\text{and} \quad 0 = \rho_f \frac{\mathrm{d}}{\mathrm{d}t} \int_{V^f} \vec{v}\, \mathrm{d}V + \rho_f \oint_{\partial(V^f)} \vec{v}\, (\vec{v} - \vec{v}_g) \cdot \mathrm{d}\vec{S} + \oint_{\partial(V^f)} p\boldsymbol{I} \cdot \mathrm{d}\vec{S} - \oint_{\partial(V^f)} \boldsymbol{\tau}_f \cdot \mathrm{d}\vec{S}, \tag{3}$$

along with boundary conditions

$$p(x_{\text{is}} = -T_{\text{entry}} - T) = p_{\text{in}}(t) \tag{4}$$

$$p(x_{\text{is}} = T_{\text{exit}}) = 0, \tag{5}$$

$$\vec{v}(x_{\text{ap}} = \pm L/2) = \vec{v}_g(x_{\text{ap}} = \pm L/2) = 0, \tag{6}$$

$$\text{and} \qquad \vec{v}(x_{\text{ml}} = \pm W/2) = \vec{v}_g(x_{\text{ml}} = \pm W/2) = 0, \tag{7}$$

with p the fluid pressure, $\vec{v}_g$ the discretized grid velocity and $p_{\text{in}}(t)$ the time-varying pressure at the inlet

$$p_{\text{in}}(t) \equiv p_{\max} \begin{cases} (t/t_0)^2[3 - 2\,(t/t_0)] & \forall t \in [0, t_0] \\ 1 & \forall t \in [t_0, \infty) \end{cases} \tag{8}$$

where $p_{\max} = 400$ Pa and $t_0 = 0.150$ s. Zero pressure at the outlet and no-slip and no-penetration at all bounding surfaces except the inlet and outlet are enforced. Here $\vec{v}$ represents the fluid velocity, V^f the volume of the fluid domain, $\partial(V^f)$ its bounding surface, p the fluid pressure, $\boldsymbol{I}$ the second-order identity tensor, $\boldsymbol{\tau}_f$ the surface traction vector on the fluid boundary. The operator $\cdot$ represents a tensor contraction and the operator ∇ the gradient vector. The motion of the moving–deforming glottal surface given by the grid velocity $\vec{v}_g$ is determined by the FSI model (described later). The fluid volume is discretized using tetrahedral cells, with a minimum cell size of 0.050 mm near the glottis ensured throughout the computation. The fluid model is implemented in ANSYS/Fluent (ANSYS Fluent Release 12.0 User Guide, 2009). The solution is advanced in time following the implicit PISO (Pressure Implicit with Splitting of Operator) algorithm with neighbor and skewness correction (Issa, 1986).

The VF domain comprises identical and disjoint left and right solid parts (figure 1b shows the left VF). Both VFs have a depth $D = 8.40$ mm separated intially by $d_g = 0.600$ mm. VF mechanics is governed by the principle of virtual work (Zienkiewicz et al., 2005)

$$\int_{V^s} \boldsymbol{\sigma} : \delta \boldsymbol{D}_v \, \mathrm{d}V = \oint_{\partial(V^s)} \boldsymbol{\tau_s} \cdot \delta \vec{u}_v \, \mathrm{d}S - \int_{V^s} \rho_s \ddot{\vec{u}} \cdot \delta \vec{u}_v \, \mathrm{d}V. \tag{9}$$

with $\boldsymbol{\sigma}$ the Cauchy stress, V^s the solid volume, $\boldsymbol{\tau_s}$ the traction applied on the boundary $\partial(V^s)$, ρ_s the uniform solid density, $\vec{u}$ the solid displacement, $\boldsymbol{D} = \nabla \vec{u}$ the displacement gradient, δ a variation of the virtual variables (subscripted 'v'), operator : the double-contraction of two tensors, accent-marks $\dot{}$ and $\ddot{}$ respectively the first- and second-order time-derivatives and ν the Poisson's ratio. The VF constitutive behavior is isotropic linear viscoelastic with $\boldsymbol{\sigma}$ depending on the history of the deviatoric strain rate $\dot{\boldsymbol{e}}$ and bulk strain rate $\dot{\epsilon}$

$$\boldsymbol{\sigma}(t) = \int_0^t 2G(t - t')\dot{\boldsymbol{e}} \, \mathrm{d}t' + \boldsymbol{I} \int_0^t K(t - t')\dot{\epsilon} \, \mathrm{d}t' \tag{10}$$

The time dependence of the shear and bulk moduli are

$$G(t) = \frac{E}{2(1+\nu)}\left[1 - g_1 + g_1 \mathrm{e}^{-t/\tau_1}\right], \tag{11}$$

$$\text{and} \quad K(t) = \frac{E}{3(1-2\nu)}\left[1 - k_1 + k_1 \mathrm{e}^{-t/\tau_1}\right] \tag{12}$$

The viscoelastic relaxation is modeled by shear and bulk relaxation factors $g_1 = 0.100$ and $k_1 = 0.100$ respectively and relaxation time-constant $\tau_1 = 0.100$ s. The elastic modulus E varies in the *ap* direction as

$$E(x_{\mathrm{ap}}) = E_0 + E_1 f(x_{\mathrm{ap}}) \tag{13}$$

with $E_0 = 6.00$ kPa and $E_1 f(x_{\mathrm{ap}})$ an *ap*-variation around it (detailed in section 2.2). The tissue is assumed to be nearly incompressible ($\nu = 0.450$) and having density $\rho_s = 1070$ kg/m^3. The VF volumes are discretized using first-order hexahedral elements with minimum edge length 0.110 mm near the medial surface where the maximum deformation is expected. For further reference a line AB oriented in the *ap* direction and lying on the left VF surface and a nodal location $\mathbf{X}_{MC}$ corresponding to the mid-point of AB are defined (figure 1b). Boundary conditions

$$\vec{u}(x_{\mathrm{ap}} = \pm L/2) = 0, \qquad \vec{u}(x_{\mathrm{ml}} = \pm W/2) = 0 \tag{14}$$

constrain all degrees of freedom on the lateral, anterior and posterior surfaces. Displacement and traction boundary conditions on the glottal surfaces (left VF: S_L, right VF: S_R, figure 1c) are determined from the FSI model. The solid domain model is implemented in Abaqus/Standard (Abaqus Version 6.11 Documentation, 2011). The solution is integrated implicitly in time using the Hilber–Hughes–Taylor algorithm (Hilber et al., 1977).

The FSI model defines the interaction between the glottal surfaces on the VF domain and the glottal surface of the airflow domain. The FSI model applies the traction boundary condition (called the dynamic boundary condition)

$$\boldsymbol{\tau}_s = (-p\boldsymbol{I} + \boldsymbol{\tau}_f) \cdot \hat{n}. \tag{15}$$

ensuring equal and opposite tractions acting on the domains of glottal surfaces in both model parts. Terms on the left and right sides of (15) are evaluated by interpolating between neighbouring nodes taken from the VF and airflow models respectively. The FSI model computes the grid velocity of the glottal surfaces in the airflow model from the kinematic boundary condition $\vec{v}_g = \dot{\vec{u}}$ where $\dot{\vec{u}}$ is evaluated on S_L and S_R. The deformed glottal surface geometries in the airflow and VF models always remain coincident. The dynamic and the kinematic boundary conditions are applied at intervals of 50 µs, which equals the fixed time-increment of both the flow and solid domain solvers. The FSI model is implemented in MpCCI version 4.1 (Joppich and Kürschner, 2006).

Table 1: Modulus distribution function $f(x_{\text{ap}})$.

x_{ap} [mm]	-10.0	-6.10	-2.40	-0.10	1.40	2.40	5.90	10.0
$f(x_{\text{ap}})$	-0.711	-0.711	0.154	3.18	0.154	0.731	-0.711	-0.711

2.2. Parametric study of gradients in elastic modulus

A spatially varying function $E(x_{\text{ap}})$ is used to define the VF elastic modulus (13). The average elastic modulus $E_0 = 6$ kPa is based on the *ap* elastic modulus of the lamina propria (comprising the cover and ligament layers) measured by Zhang et al. (2009). The *ap*-variation of $E(x_{\text{ap}})$ is modeled by $f(x_{\text{ap}}) \equiv (E_l - \bar{E}_l)/\bar{E}_l$, where the *ap*-graded elastic modulus E_l (with an average value $\bar{E}_l = 182$ kPa) was measured from an excised vocal ligament of a 60 year old male subject (Kelleher et al., 2010). From the measurements of Kelleher et al. (2010) $f(x_{\text{ap}})$ is computed (table 1) and a piecewise-linear fit is plotted in figure 2. In (13) E_1 represents the magnitude of VF modulus gradation. In this study the value of E_1 is varied parametrically. In case 1, $E_1 = 0$ kPa represents a homogeneous distribution, in case 2 an intermediate value $E_1 = 3$ kPa is used and finally in case 3, $E_1 = 6.00$ kPa ($= E_0$) creates a distribution with high heterogeneity. E_0 is identical across the three cases.

2.3. Modal analysis of in vacuo and FSI dynamics

Modal analysis of in vacuo VF dynamics is frequently used to characterize VF oscillatory behavior. It suffices to analyze only the left VF since both VFs possess identical geometry and material properties. In this analysis the boundary conditions constraining all degrees of freedom on the lateral, anterior and posterior VF surfaces remain identical to those in the FSI analysis (14), but the surface S_L is stress-free since fluid excitation is absent. Viscoelasticity of the VF tissue is ignored in this analysis. Modal analysis gives in vacuo eigenfrequencies (also known as natural frequencies) and eigenmodes.

On the other hand, VF motion in FSI is controlled by fluid loading. A well-known method for analyzing dynamic data, such as from FSI, is proper orthogonal decomposition (POD). POD analysis is conducted for only the left glottal surface displacements, thereby neglecting left-right asymmetries in VF motion. Left VF displacement data is used to populate a matrix, with rows corresponding to 3060 glottal surface nodes and columns corresponding to over 30 distinct time instants within a given vibration cycle. Singular value decomposition of the matrix yields for every k-th FSI mode an eigenvalue $\alpha^{(k)}$ and corresponding modes shapes $\vec{h}^{(k)}(\vec{x})$ (spatial) and $g^{(k)}(t)$-s (temporal). FSI modes are numbered by the descending order of their eigenvalues. Only the first three FSI modes were analyzed. The spatio-temporal variation of VF displacement is approximated as

$$\vec{u}(\vec{x}, t) \simeq \sum_{k=1}^{3} \alpha^{(k)} \vec{h}^{(k)}(\vec{x}) g^{(k)}(t). \tag{16}$$

Table 2: Influence of elastic gradients on FSI frequency F_0 and medial–lateral displacement at mid-coronal location $u_{\mathrm{ml}}(\mathbf{X}_{MC})$ averaged over multiple vibration cycles (with standard deviations SD), and on the first three FSI eigenvalues $\alpha^{(k)}$ $(k = 1 \ldots 3)$ obtained from POD analysis of vibration cycles specified by start and end time instants t_{start} and t_{end} respectively.

Case	1	2	3
F_0 [Hz]	108 (SD 4.18 %)	109 (SD 4.95 %)	153 (SD 3.48 %)
$u_{\mathrm{ml}}(\mathbf{X}_{MC})$ [mm]	−0.212	−0.198	−0.201
t_{start} [s]	0.2538	0.1968	0.2838
t_{end} [s]	0.2639	0.2054	0.2900
$\alpha^{(1)}$	0.349	0.210	0.212
$\alpha^{(2)}$	0.106	0.027	0.018
$\alpha^{(3)}$	0.050	0.019	0.015

Parseval's identity states that the square of $\alpha^{(k)}$ divided by the sum of squares of all $\alpha^{(k)}$-s is the fraction of the total spatio-temporal variation of displacement explained by the k-th FSI mode.

3. Results

3.1. in vacuo eigenmodes

The first three in vacuo eigenfrequencies (natural frequencies) are: in case 1, 48.2 Hz, 65.6 Hz and 79.1 Hz; in case 2, 53.2 Hz, 64.6 Hz and 78.7 Hz; and in case 3, 47.7 Hz, 50.3 Hz and 61.0 Hz. Across cases 1–3 the first eigenfrequency varies only slightly from 47.7 to 53.2 (10.9 % difference). This correspondence is maintained between cases 1 and 2 even for the next two eigenfrequencies (difference not exceeding 1.54 %) which are somewhat higher than the respective eigenfrequencies of case 3.

3.2. Local glottal surface motion characteristics in FSI

The *ml* displacement of location $\mathbf{X}_{MC}$ with time ($u_{\mathrm{ml}}(\mathbf{X}_{MC})$) is considered to be representative of the motion of the left VF. Table 2 compares overall vibration characteristics for multiple cycles corresponding to cases 1–3. Average $u_{\mathrm{ml}}(\mathbf{X}_{MC})$ does not differ significantly across the cases (SD 3.62 %). This is expected since the stiffness of the VFs is on average identical across the cases. Vibration cycles are defined to start and end at consecutive peaks of $u_{\mathrm{ml}}(\mathbf{X}_{MC})$ in time. The phonation frequency F_0 was obtained as

$$F_0 = \frac{1}{t_{\mathrm{cycle}}}, \tag{17}$$

where t_{cycle} separates two consecutive peaks of $u_{\mathrm{ml}}(\mathbf{X}_{MC})$. The average F_0 is significantly different in case 3. In each case F_0 has no apparent correspondence with the first three eigenfrequencies noted earlier. For

case 1, the net mass flow rate through the outlet averaged 0.676 g/s, and oscillated with a frequency of 108 Hz (similar to F_0).

Next, consider one particular cycle of vibration in each of the cases 1–3. Table 2 gives corresponding to each cycle, the cycle start and end times t_{start} and t_{end} respectively. Within each cycle, four representative time instants are identified. Two of these instants correspond to times when $u_{\text{ml}}(\mathbf{X}_{MC})$ attains the minimum and maximum value over the vibration cycle. Since negative values of $u_{\text{ml}}(\mathbf{X}_{MC})$ correspond to an opening of the glottal gap, the above instants can respectively be taken to represent the open and closed states of the VF. At the other two instants, $u_{\text{ml}}(\mathbf{X}_{MC})$ has intermediate values. One instant is in the closing phase while the other is in the opening phase.

Figure 3a,b shows the variation of *is* and *ml* displacement components along the *ap* line AB at the four representative instants for case 1. Plots for case 2 and 3 are given in figures 3c,d and 3e,f. The location $\mathbf{X}_{MC}$ corresponds to $x_{\text{ap}} = 0$. Closed and open instants and the intermediate instants are distinguished in these figures. Net mass flow rates through the outlet in dependence of time are shown.

3.3. POD analysis

Table 2 gives the first 3 FSI eigenvalues from a POD analysis. In each case POD analysis is performed on the displacements corresponding to the vibration cycle selected above. From Parseval's identity the first three FSI modes were found to explain at least 99.8 % of the spatio-temporal variation of the displacement during the cycle. Excluding the variation explained by FSI mode 1, the remainder is explained up to 99.0 %, 93.7 % and 90.6 % respectively in cases 1, 2 and 3 by FSI modes 2 and 3 combined. Figures 4 and 5 respectively show the spatial and temporal variation of the FSI-modes. In order to facilitate comparison, both $\vec{h}^{(k)}$ and $g^{(k)}$ are normalized to lie within $[-1, 1]$. The correlation between FSI modes and in vacuo eigenmodes is given in table 3.

3.4. Airflow

Figure 6a shows the variation of mass-flow rate with time for the selected vibration cycle in each case. In order to facilitate comparison both mass flow rate and time ranges are normalized to lie in the unit interval (figure 6b).

Figure 7 shows, at closed and open states, the region of the glottal jet possessing a high vorticity magnitude ($|\omega| = |\nabla \times \vec{v}| \geq 10^4$ s^{-1}). The jet region boundary is colored by contours of velocity magnitude $|\vec{v}|$.

4. Discussion

The in vacuo frequencies for case 1 (no elastic gradients) compare excellently with those determined by Zhang (2011) for a nearly identical VF model. The small differences are attributed to $E_0 = 4$ kPa in Zhang

Table 3: Square of correlation R^2 between FSI-modes and in vacuo eigenmodes. A dash indicates a value smaller than 0.001.

		in vacuo mode 1	in vacuo mode 2	in vacuo mode 3
Case 1	FSI mode 1	0.945	–	0.132
	FSI mode 2	0.006	0.003	0.015
	FSI mode 3	0.092	0.013	0.064
Case 2	FSI mode 1	0.920	–	0.144
	FSI mode 2	0.008	0.042	0.031
	FSI mode 3	0.032	0.031	0.034
Case 3	FSI mode 1	0.872	0.014	0.136
	FSI mode 2	–	0.018	0.017
	FSI mode 3	0.001	0.162	–

(2011) as against 6 kPa in this paper. Since E_0 is fixed for cases 1–3, the first in vacuo eigenfrequency and the average displacement (during FSI) are independent of elastic gradients (table 2). However, elastic gradients strongly influence the phonation frequency F_0 in FSI (table 2). This follows the argument of Zhang et al. (2007) that F_0 is dependent on a flow-induced stiffness. The complexity of the flow–structure interaction perhaps justifies the non-linear increase in F_0 from case 1 to case 3.

Average F_0 (table 2), *ml* displacement (table 2) and net mass-flow rate through the glottis were within the range of observations in experimental studies conducted with similar VF and glottal tract geometry (Alipour and Scherer, 1995; van den Berg et al., 1957; Cranen and Boves, 1985; Erath and Plesniak, 2006, 2010; George et al., 2008; Morris and Brown Jr., 1996; Scherer et al., 2001; Thomson et al., 2005; Titze, 2006; Triep et al., 2005; Triep and Brücker, 2010; Zhang et al., 2006).

Considering the variation of *is* displacement along AB at different instants (figures 3a,c,e), the average deformed shape goes from an inverted-U shape in case 1 to an M shape in case 3. The increase in gradient of elastic modulus from case 1 to 3 is associated with a decrease in stiffness near the anterior and posterior ends and an increase in stiffness in the mid-membranous region. This causes more bulging near the ends than in the middle section. A similar behavior was predicted in Kelleher et al. (2010) where the analysis was based on a study of in vacuo mode shapes. The time-dependence of the deformed shape is obtained uniquely in FSI and is analyzed further below.

In the insets of figure 3 the mass-flow rate is plotted throughout the vibration cycle from which the displacement graphs in figure 3 are obtained. Though the frequency of oscillation of mass-flow rate and of $u_{\mathrm{ml}}(\mathbf{X}_{MC})$ were very close to each other, there exists a noticeable phase difference between the two. The phase difference can be attributed to the 3D nature of VF vibration, i.e. the net mass flow rate depends

on u_{ml} at more than one *ap* location. In cases 1 and 2, the flow rate leads the displacement, whereas the situation is reversed in case 3. In case 3, u_{ml} plotted along line AB at different instants within a vibration cycle (figure 3f) suggest that while the mid-membranous region is in closing phase, a slightly off-center location could be in the opening phase. This can substantially alter the dynamics of the glottal jet, and in particular the phase difference.

Focusing on FSI mode 1, table 2 shows that in each case this mode has the highest eigenvalue, implying most of the deformation of the VF is captured by FSI mode 1. Figure 5 shows that the temporal variation of FSI mode 1 is negligible, with $g^{(1)}(t)$ possessing values close to -1. Hence, the FSI mode 1 describes the non-oscillating part of deformation. The FSI mode 1 shape (figure 4), after multiplying with the -1 factor, captures well the average upward bulge of the VF around which further oscillation takes place. This also agrees with the average *is* displacement (figures 3a,c,e). In each case, the variation in FSI mode 1 is explained most by in vacuo modes 1 and 3, in order.

Figure 4 shows FSI mode 2 characterized by oscillatory bulging out and shrinking in of the glottal surface, primarily in the *ml* direction. Going from the homogeneous VF (case 1) to the highly graded VF (case 3), the peak bulge location shifts from a mid-coronal position to two increasingly separated anterior and posterior positions. This agrees with the variation of u_{ml} along AB (figures 3b,d,f), and is explained directly by the variation of $E(x_{\mathrm{ap}})$ across the three cases.

FSI mode 3 causes an upward bulge varying in the *ml* direction. While the lateral regions dip down, the medial surface lifts up, and vice versa. As in the case of other FSI mode shapes, the coronal plane at which the downward dip and upward lift are maximum moves from a mid-coronal location in case 1 and splits into two anterior and posterior located coronal planes in case 3.

Figure 5 indicates that in each case $g^{(k)}(t)$ is on average zero for FSI modes 2 and 3 implying a purely oscillatory behavior. The frequency of oscillation with time equals F_0. Interestingly $g^{(2)}(t)$ leads $g^{(3)}(t)$ by 90° in cases 1 and 2, but then lags by the same phase in case 3.

After excluding the part explained by FSI mode 1, a decreasing fraction of VF dynamics is explained by FSI modes 2 and 3 combined as one goes from case 1 to case 3. This suggests that increase in VF elastic gradients leads to an increase of the number of distinct FSI modes recruited in VF oscillation, and thereby to an increase in spectral width of the oscillation signal.

For all 3 cases, the variation in FSI modes 2 and 3 explained by the first three in vacuo eigenmodes is below 17 % (table 3). This indicates that higher order in vacuo modes make significant contributions to FSI modes 2 and 3. For FSI mode 3 in case 1, the first and third in vacuo eigenmode make higher contributions than the second in vacuo eigenmode. These relative contributions to FSI mode 3 tend to become more uniform in case 2. Finally in case 3 a complete reversal is achieved: the in vacuo mode 2 makes a higher contribution to FSI mode 3 than the in vacuo modes 1 and 3.

Comparing the in-cycle mass flow rate (figure 6a) in cases 1 and 2, it is clear that the fluctuation amplitude

(or contrast) of the flow is higher for case 2 with higher gradient. This emphasises the importance of a more trapezoidal opening in case 2 as mentioned before. This confirms a similar prediction made in Kelleher et al. (2010) following a linear eigenmode analysis.

The normalized waveforms in figure 6b suggest that a higher gradient of elastic modulus can induce differences in the spectrum of harmonic excitation provided by the airflow output. This agrees with the previous observation that increase in gradients of elastic modulus increase the spectral width of VF dynamics in FSI. Flow rates in cases 1 and 2 have a noticeably different spectral-width than the flow rate in case 3. Since collision between the VFs was not considered, the LF pattern (Fant and Liljencrants, 1985) is not apparent. Rather the airflow curves are similar to those obtained for breathy voice (Hillenbrand and Houde, 1996).

Figure 7 demonstrates the effect of VF vibration shapes on the glottal jet shape. The jet structure changes significantly in the closed state. Especially in cases 2 and 3, the *ap* asymmetry in displacements caused by the gradients in elastic modulus is reflected in the jet passing through the glottis. In case 1 the flow is reduced in the mid-membranous region, resulting the jet to split in the closed state. However in cases 2 and 3, the jet is preferentially aligned to one side along the *ap* direction. The Coanda effect is well documented in VF flows, and is known to cause the jet to move in the *ml* direction. In this study, the Coanda effect was observed though it is not shown here. The *ap* asymmetry of the jet (expected to be substantial when gradients in elastic modulus exist) along with the Coanda effect will cause the glottal jet to have an exceedingly high 3D character.

5. Conclusion

This study was conducted to investigate the role of gradients in elastic modulus on VF dynamics and airflow. Elastic modulus variation along the *ap* direction of the vocal ligament, obtained by careful measurements based on digital image correlation, were used to inform a full 3D VF tissue model. Specifically, elastic modulus within the VF tissue possessed a variation similar to that measured in the ligament, but the average modulus was based on a study that measured the average modulus of the lamina propria. An FSI investigation was conducted with three models with successively increasing gradients in elastic modulus. A study on the effect of elastic modulus gradients has never been attempted before, and hence the present results provide novel insights.

An important observation is that changes in gradients of elastic modulus alter the phonation frequency in a highly non-linear fashion. An increase in the gradient can lead to the following changes in VF dynamics,

- a more trapezoidal deformed shape of the VF in the *is* direction,
- higher amplitude of vibration at off-mid-membranous locations,

- increased *ap* asymmetry in *is* and *ml* displacements, and
- *ap* mucosal waves (see supplementary material).

POD analysis of VF dynamics suggests that elastic gradients influence

- the number of distinct FSI modes recruited in vibration
- the phase relationship between the modes
- the correspondence of FSI modes with in vacuo eigenmodes

These changes are concomitant with following alterations in glottal flow

- higher contrast of glottal airflow output,
- increase in spectral-width of glottal airflow output, and
- strong *ap* asymmetry of the glottal jet.

Phonation frequency, contrast and spectral-width of glottal airflow output and glottal jet dynamics influence speech quality significantly (Rotherberg, 1981; Titze and Story, 1997). The present study demonstrates a strong link between gradients in elastic modulus and speech quality.

The main limitations of this study arise out of modeling simplifications. The distribution of elastic modulus within the length of the ligament was used as a model for the distribution within the entire VF tissue. Kelleher et al. (2012) found this distribution itself changes in cover and ligament layers. Future studies conducted with layered VF tissue models could provide further insights. Determining the sensitivity to functional gradation in the presence of anisotropy could be interesting. The present study did not consider collision between the vocal folds, but this is no principal limitation. Yet, gradients in elastic modulus can be expected to play a significant role in modifying stress distributions within the VF tissue under collision conditions.

Conflict of interest statement

The authors of this manuscript have no conflicts of interest related to the content of the study.

Acknowledgement

The study was funded by the NIDCD Grant 5R01DC008290-04.

Abaqus Version 6.11 Documentation, 2011. Dassault Systémes Simulia Corp.,. Providence, RI, USA .

Alipour, F., Scherer, R.C., 1995. Pulsatile airflow during phonation: an excised larynx model. J. Acoust. Soc. Am. 97, 1241–1248.

ANSYS Fluent Release 12.0 User Guide, 2009. ANSYS Inc.,. Canonsburg, PA, USA .

van den Berg, J., Zantema, J.T., Doornenbal Jr., P., 1957. On the air resistance and the Bernoulli effect of the human larynx. J. Acoust. Soc. Am. 29, 626–631.

Bhattacharya, P., Siegmund, T., 2014a. Computational modeling of vibration-induced systemic hydration of vocal folds over a range of phonation conditions. International Journal for Numerical Methods in Biomedical Engineering .

Bhattacharya, P., Siegmund, T., 2014b. A computational study of systemic hydration in vocal fold collision. Computer Methods in Biomechanics and Biomedical Engineering 17, 1835–1852.

Bhattacharya, P., Siegmund, T., 2014c. Validation of a flow-structure-interaction computation model of phonation. Journal of Fluids and Structures 48, 169–187.

Bhattacharya, P., Siegmund, T., 2015. The role of glottal surface adhesion on vocal folds biomechanics. Biomech. Model. Mechan. 14, 283–295.

Cranen, B., Boves, L., 1985. Pressure measurements during speech production using semiconductor miniature pressure transducers: Impact on models for speech production. J. Acoust. Soc. Am. 77, 1543–1551.

Erath, B.D., Plesniak, M.W., 2006. The occurrence of the Coanda effect in pulsatile flow through static models of the human vocal folds. J. Acoust. Soc. Am. 120, 1000–1011.

Erath, B.D., Plesniak, M.W., 2010. An investigation of asymmetric flow features in a scaled-up driven model of the human vocal folds. Exp. Fluids 49, 131–146.

Fant, G., Liljencrants, J., 1985. A four parameter model of the glottal flow. STL-QPSR 26, 1–13.

George, N.A., de Mul, F.F.M., Qiu, Q., Rakhorst, G., Schutte, H.K., 2008. Depth-kymography: high-speed calibrated 3d imaging of human vocal fold vibration dynamics. Physics in Medicine and Biology 53, 2667–2675.

Hilber, H.M., Hughes, T.J.R., Taylor, R.L., 1977. Improved numerical dissipation for time integration algorithms in structural dynamics. Earthq. Eng. Struct. D. 5, 283–292.

Hillenbrand, J., Houde, R.A., 1996. Acoustic correlates of breathy vocal quality: dysphonic voices and continuous speech. J. Speech Hear. Res. 39, 311–321.

Issa, R.I., 1986. Solution of the implicitly discretized fluid flow equation by operator splitting. J. Comput. Phys. 62, 40–65.

Joppich, W., Kürschner, M., 2006. MpCCI – a tool for the simulation of coupled applications. Concurrency Computat.: Pract. Exper. 18, 183–192.

Kelleher, J.E., Siegmund, T., Chan, R.W., 2012. Could spatial heterogeneity in human vocal fold elastic properties improve the quality of phonation? Annals of Biomedical Engineering 40, 2708–2718.

Kelleher, J.E., Zhang, K., Siegmund, T., Chan, R.W., 2010. Spatially varying properties of the vocal ligament contribute to its eigenfrequency response. J. Mech. Behav. Biomed. Mat. 3, 600–609.

Morris, R.J., Brown Jr., W.S., 1996. Comparison of various automatic means for measuring mean fundamental frequency. J. voice 10, 159–165.

Rotherberg, M., 1981. Acoustic interaction between the glottal source and the vocal tract, in: Stevens, K.N., Hirano, M. (Eds.), Vocal fold physiology. University of Tokyo Press. chapter 21, pp. 305–328.

Scherer, R.C., Shinwari, D., DeWitt, K.J., Zhang, C., Kucinschi, B.R., Afjeh, A.A., 2001. Intraglottal pressure profiles for a symmetric and oblique glottis with a divergence angle of 10 degrees. J. Acoust. Soc. Am. 109, 1616–1630.

Thomson, S.L., Mongeau, L., Frankel, S.H., 2005. Aerodynamic transfer of energy to the vocal folds. J. Acoust. Soc. Am. 118, 1689–1700.

Titze, I., 2006. The myoelastic aerodynamic theory of phonation. NCVS, Iowa City, Iowa.

Titze, I.R., Story, B.H., 1997. Acoustic interactions of the voice source with the lower vocal tract. J. Acoust. Soc. Am. 101, 2234–2243.

Triep, M., Brücker, C., 2010. Three-dimensional nature of the glottal jet. J. Acoust. Soc. Am. 127, 1537–1547.

Triep, M., Brücker, C., Schröder, W., 2005. High-speed PIV measurements of the flow downstream of a dynamic mechanical model of the human vocal folds. Exp. in Fluids. 39, 232–245.

Zhang, K., Siegmund, T., Chan, R.W., 2009. Modeling of the transient responses of the vocal fold lamina propria. J. Mech. Behav. Biomed. Materials 2, 93–104.

Zhang, Z., 2011. Restraining mechanisms in regulating glottal closure during phonation. J. Acoust. Soc. Am. 130, 4010–4019.

Zhang, Z., Neubauer, J., Berry, D.A., 2006. The influence of subglottal acoustics on laboratory models of phonation. J. Acoust. Soc. Am. 120, 1558–1569.

Zhang, Z., Neubauer, J., Berry, D.A., 2007. Physical mechanisms of phonation onset: A linear stability analysis of an aeroelastic continuum model of phonation. J. Acoust. Soc. Am. 122, 2279–2295.

Zienkiewicz, O.C., Taylor, R.L., Zhu, J.Z., 2005. Generalization of the finite element concepts. Galerkin-weighted residual and variational approaches, in: The Finite Element Method: Its Basis and Fundamentals. Butterworth–Heinemann. chapter 3, 6th edition. pp. 54–102.

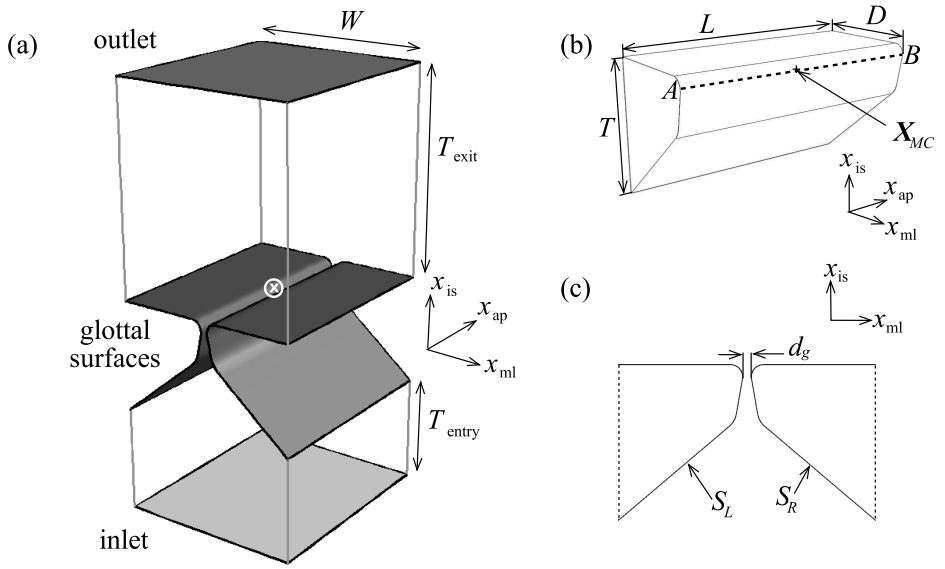

Figure 1: (a) Geometry of the glottal airflow domain: the inlet, outlet and glottal surfaces are shaded, the coordinate origin (at the intersection of the mid-coronal plane, the mid-saggital plane and the VF superior surface) is $\otimes$; (b) geometry of the left half of the solid VF model: line AB and point $\mathbf{X}_{MC}$ are reference regions at which the VF motion is characterized in this paper; (c) mid-coronal section showing both pairs of VFs and rigid planes: coordinate axes are offset from the origin for clarity

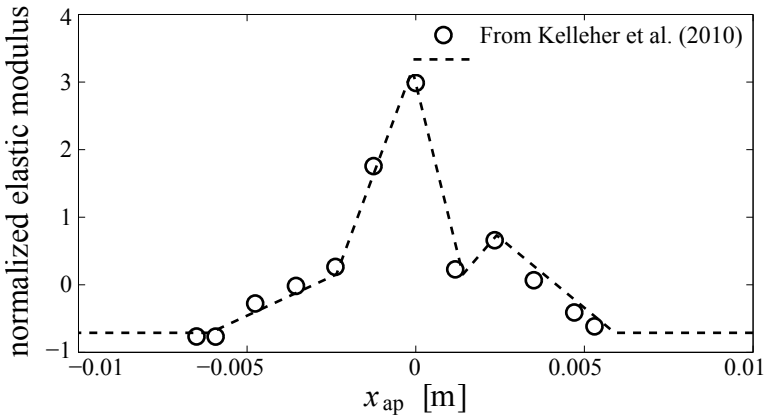

Figure 2: Piecewise linear fit to normalized elastic modulus $f(x_{\mathrm{ap}})$ in dependence of anterior–posterior location x_{ap}. Circles correspond to values in table 1.

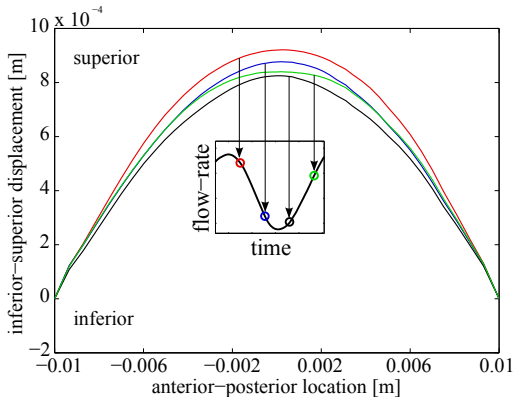

(a) case 1

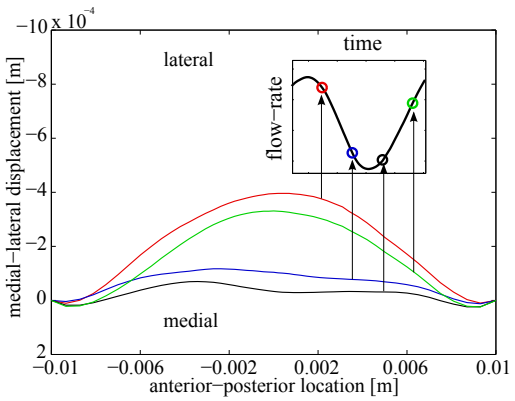

(b) case 1

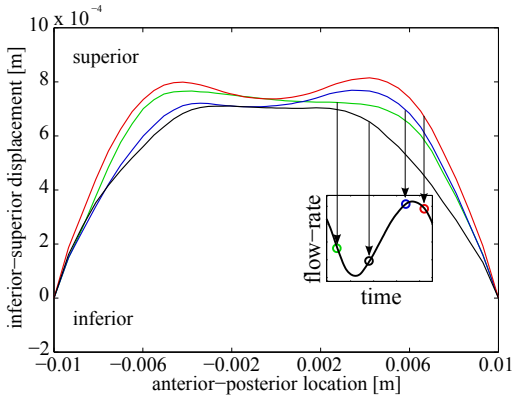

(c) case 2

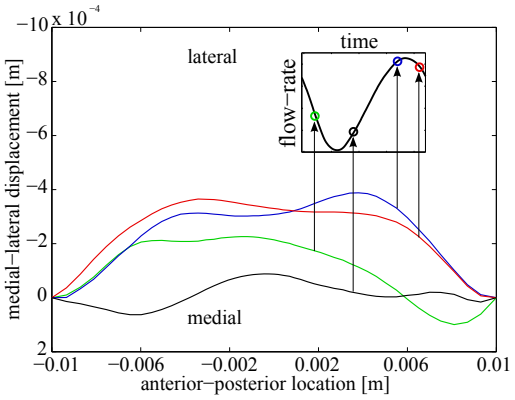

(d) case 2

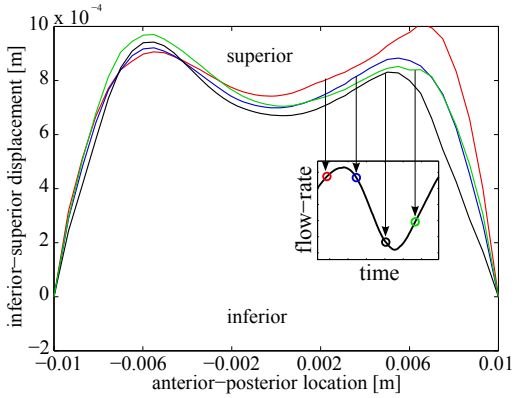

(e) case 3

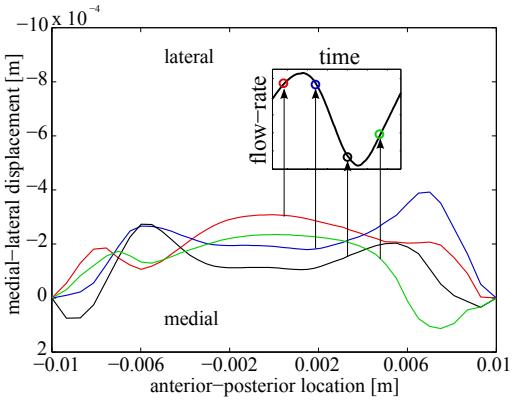

(f) case 3

Figure 3: Displacements in inferior–superior (a,c,e) and medial–lateral (b,d,f) directions plotted along line AB at 4 instants of a vibration cycle. A more open VF configuration corresponds to a more positive inferior–superior displacement and a more negative medial–lateral displacement.

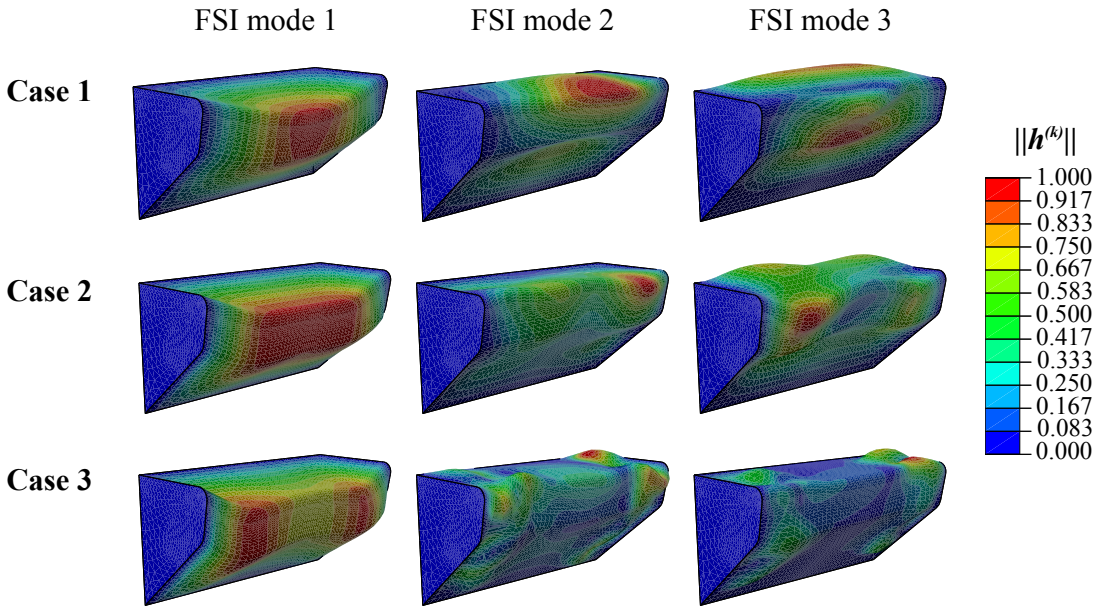

Figure 4: Spatial variation of $\vec{h}^{(k)}$ for FSI-modes $k = 1 \ldots 3$. The variation is normalized by the maximum magnitude of $\vec{h}^{(k)}$.

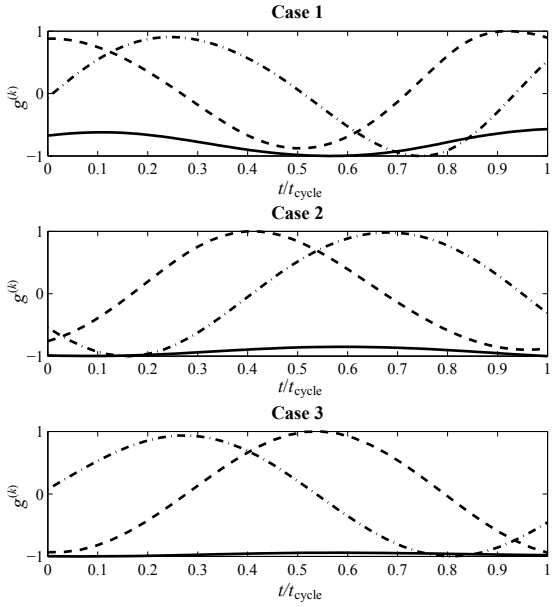

Figure 5: Temporal variation of $g^{(k)}$ for FSI-modes $k = 1 \ldots 3$: –, $k = 1$; - -, $k = 2$; -·-, $k = 3$. The scalar function $g^{(k)}(t)$ is normalized with respect to its maximum occuring magnitude.

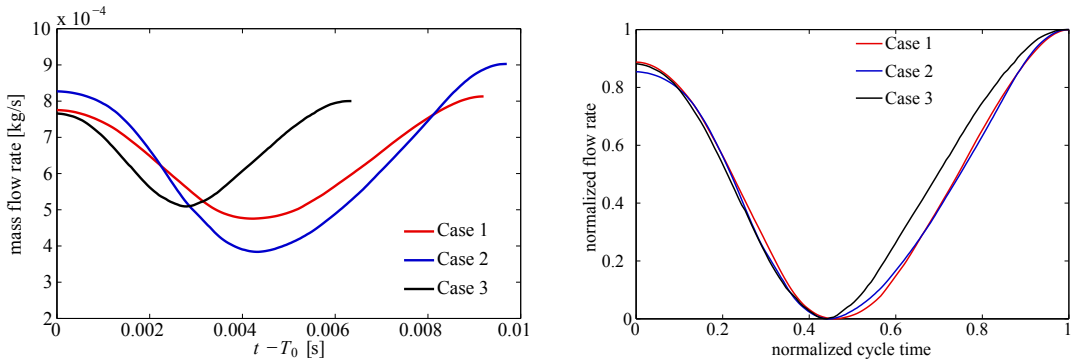

(a) (b)

Figure 6: (a) Mass flow rate in dependence of time over one vibration cycle. Time origin is at the start time t_{start} of the corresponding cycle. (b) Curves in (a) normalized such that flow rate and cycle time are in $[0, 1]$.

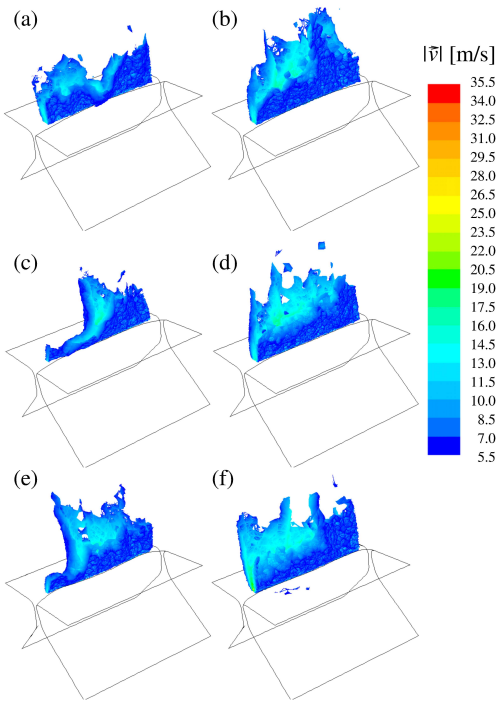

Figure 7: Velocity magnitude contours in the glottal jet: (a,b) case 1; (c,d) case 2; (e,f) case 3; (a,c,e) closed states; (b,d,f) open states.